Non-linear spirals in the Taylor–Couette problem

J. Antonijoan
*Departament Matemàtica i Telemàtica, Universitat Politècnica de Catalunya, Av. Víctor Balaguer s/n,
08800 Vilanova i la Geltrú, Spain*

F. Marquès and J. Sánchez
*Departament Física Aplicada, Universitat Politècnica de Catalunya, c/ Gran Capità s/n, Mod
B5 Campus Nord, 08034 Barcelona, Spain*

We examine non-linear spiral flow in the Taylor–Couette problem for a wide gap with axially periodic conditions. We present a highly efficient computational method adapted to this problem, based on continuation methods applied to a pseudospectral discretization of the Navier–Stokes equations in a rotating frame of reference. The spiral flow is computed in a wide range of parameters, and different features are explored in detail: domain of existence of the flow, behavior for high Reynolds number, appearance of axial flows, dependency on parameters, and stability against helical disturbances. A first integral is obtained and used to describe the particle trajectories in the fluid. This description shows that the axial and radial motion of the particles is mainly confined within an internal boundary layer. © *1998 American Institute of Physics.*
[S1070-6631(98)01604-3]

I. INTRODUCTION

The Taylor–Couette problem has been the subject of many experimental and theoretical investigations since its origins at the end of last century. Tagg's compilation[1] of literature related to the problem containing nearly 1500 references, is a good indicator of the attention it has received. Much of this work deals with the stability of the basic Couette flow. From the linear stability analysis many authors have obtained amplitude equations to perform a weakly non-linear analysis; Stuart,[2] Davey,[3] Reynolds and Potter,[4] Kirchgässner and Sorger[5] and others when the two cylinders rotate in the same direction or the outer one is at rest, and Edwards *et al.*[6] and others in the counter-rotating case. Other authors (Iooss,[7] Demay & Iooss,[8] Chossat & Iooss,[9] and others) have used center-manifold reductions of the Navier–Stokes equations or the theory of bifurcations in the presence of symmetries to deduce reduced equations to be studied. With these tools secondary and tertiary bifurcations have been predicted that qualitatively reproduce the behavior found in the experiments.

Many of these studies are restricted to small supercritical Reynolds numbers and cannot predict accurately the critical Reynolds numbers for which new bifurcations appear. It is therefore necessary to calculate solutions of the full Navier-Stokes equations. Taylor vortex flow has been calculated by many authors; Meyer-Spasche and Keller[10,11] and Dinar and Keller[12] by continuation methods, and by Fasel and Booz[13] and Marcus[14] by time evolution.

Spiral flow (SF) has received much less attention mainly because of its three-dimensional structure which poses many more difficulties. Although they can be calculated with fully three-dimensional time evolution codes, like Marcus,[15] it is computationally expensive if an extensive parameter dependence study is to be done. Edwards *et al.*[6] and Sánchez *et al.*[16] have calculated the spiral flow assuming a helical symmetry. In this case, the 3D spiral flow is described by using only two space coordinates, and computed by time-evolving the discretized Navier–Stokes equations. Edwards *et al.*[6] have compared wave speeds with results obtained with the three-dimensional code of Marcus,[15] reporting a very good agreement. In both cases a relation between the axial and the azimuthal periodicities is imposed in advance. In this paper we wish to explore the dependence of the flow with this relation, and with respect to other parameters, mainly the angular velocities of the inner and outer cylinders.

We have used continuation methods in order to obtain the spiral flow wherever it exists. This method has two advantages with respect to time evolution; first, it is much less time consuming; second, we can compute the spiral flow whether it is stable or not. Therefore this method is very well suited for studying the stability of the SF in the future. The formulation of the problem using velocity potentials (Marquès[17]) is given in Sec. II, and in Sec. III we deal with the numerical method used for the continuation procedure. We have found that the SF exists in a much wider parameter range than is experimentally observed (Sec. IV). A limited linear stability analysis of these flows, restricted to perturbations with helical symmetry, is presented.

We have also found properties of the SF for high Reynolds numbers, showing some features similar to Taylor Vortex Flow (TVF) at high Reynolds numbers, as in Fasel and Booz.[13] A new feature is that the spiral flow in an axially periodic domain exhibits a weak but not zero axial mass flow, as has been pointed out by Edwards *et al.*[6] This is a purely non-linear effect, appearing as a result of the reflexional ($z \rightarrow -z$) symmetry breaking bifurcation from which the SF emerges (Sec. V).

The trajectories of the velocity field generated by the spiral flow are also investigated in this paper (Sec. VI). The formulation in terms of potentials for the velocity field and the incompressibility condition provide a first integral that provides a detailed description of the trajectories and an explanation for the axial mean flow.

II. FORMULATION OF THE PROBLEM

We consider the flow of an incompressible fluid confined between two concentric cylinders, of inner and outer radii r_i^*, r_o^* and gap $d = r_o^* - r_i^*$, which can rotate independently with angular velocities Ω_i, Ω_o. The non-dimensional parameters are the radius ratio $\eta = r_i^*/r_o^*$, and the Reynolds numbers associated with the tangential velocity of the cylinders $R_i = dr_i^* \Omega_i/\nu$, $R_o = dr_o^* \Omega_o/\nu$ where ν is the kinematic viscosity. We adimensionalize the equations using d, d^2/ν for space and time, respectively. The Navier–Stokes equations and the incompressibility condition then read as

$$\partial_t \mathbf{v} + \mathbf{v} \cdot \nabla \mathbf{v} = -\nabla p + \Delta \mathbf{v}, \qquad \nabla \cdot \mathbf{v} = 0, \tag{1}$$

where p is the pressure divided by the constant density of the fluid. We will assume infinite cylinders and solutions periodic in the axial direction, of period $2\pi b$.

The geometrical structure and symmetry properties of the spiral flow are well known. The book of Chossat and Iooss[9] is an excellent review of the analysis based on center manifold reduction and the corresponding amplitude equations. These methods do not supply a full description of the flow, and they are also limited to a neighborhood of the bifurcation point. Nevertheless they are very useful because they give some of the global properties—as symmetry properties—of the flow, and a qualitative picture of the bifurcation. We have taken the benefit of these properties for the formulation of our main equations and the corresponding numerical methods.

The spiral flow that appears in the counter-rotating case has a spatial structure invariant with respect to a rotation around the cylinder's axis and a simultaneous translation in the axis direction, i.e. a helical movement which we call helical symmetry (see Ref. 9). This symmetry can be written in cylindrical coordinates,

$$(r, \theta, z) \rightarrow (r, \theta + \beta, z + b\beta), \tag{2}$$

where β is the rotation angle, $2\pi b$ is the axial period, and b a constant that fixes the relative magnitude of the rotation and the translation; b is then related to the slope of the spiral pattern.

We introduce the system of coordinates,

$$x = 2r - \delta, \qquad \theta_h = \theta, \qquad \rho = z/b - \theta, \tag{3}$$

with $\delta = r_i + r_o$, $(x, \theta_h, \rho) \in [-1,1] \times [0, 2\pi] \times [0, 2\pi]$. The relationship between partial derivatives is

$$\partial_r = 2\partial_x, \qquad \partial_\theta = \partial_{\theta_h} - \partial_\rho, \qquad \partial_z = b^{-1}\partial\rho. \tag{4}$$

We have introduced x because the unknowns of the problem will be expanded in Chebyshev polynomials in the radial direction [Eqs. (15), (16)]. It is easy to see that velocity fields whose components are functions only of the coordinates r

and $\rho = z/b - \theta$, are invariant with respect to the helical symmetries described above. It must also be noted that functions 2π-periodic in ρ are 2π-periodic in θ and $2\pi b$-periodic in z. We will therefore look for solutions with $\partial_{\theta_h} = 0$. Replacing in (4), we obtain the relations $\partial_\theta = -\partial_\rho$ and $\partial_z = b^{-1}\partial_\rho$ that are used in all subsequent equations. The three-dimensional structure of the spiral flow is now described by using only two space coordinates, and the flow can be numerically computed in detail with a moderate computational cost.

The spiral flow is a traveling wave in both azimuthal and vertical directions (see Ref. 9). Therefore Navier–Stokes equations (1) are written in a rotating frame of reference with an angular velocity Ω, in which this flow is steady:

$$\partial_t \mathbf{v} + 2\Omega \hat{\mathbf{e}}_z \times \mathbf{v} + \boldsymbol{\omega} \times \mathbf{v} = -\nabla \tilde{p} + \Delta \mathbf{v}, \qquad \nabla \cdot \mathbf{v} = 0, \tag{5}$$

where $\boldsymbol{\omega} = \nabla \times \mathbf{v}$ is the vorticity field, we have used the identity $\mathbf{v} \cdot \nabla \mathbf{v} = \boldsymbol{\omega} \times \mathbf{v} + \nabla(\mathbf{v}^2/2)$, and we have included $\nabla(\mathbf{v}^2/2)$ and the centrifugal term into $\tilde{p}$. The presence of the Coriolis term is equivalent to changing the vorticity $\boldsymbol{\omega} = \nabla \times \mathbf{v}$ into $\nabla \times \mathbf{v} + 2\Omega \hat{\mathbf{e}}_z$. The Reynolds numbers in this frame change into $R_i \rightarrow R_i - \Omega r_i$, $R_o \rightarrow R_o - \Omega r_o$. The (non-dimensional) angular velocity Ω is a property of the spiral flow, and will be determined simultaneously with the flow, as will be seen later.

To solve the equations, we introduce the mean velocities in the azimuthal and axial directions as averages over ρ, and we use toroidal and poloidal potentials for the ρ-dependent velocity part,

$$\mathbf{v} = \bar{v}_\theta \hat{\mathbf{e}}_\theta + \bar{v}_z \hat{\mathbf{e}}_z + \nabla \times (\psi \hat{\mathbf{e}}_z) + \nabla \times \nabla \times (\phi \hat{\mathbf{e}}_z), \tag{6}$$

where

$$\bar{v}_\theta = P_\rho v_\theta, \quad \bar{v}_z = P_\rho v_z, \quad P_\rho F = \frac{1}{2\pi} \int_0^{2\pi} F(r, \rho, t) d\rho. \tag{7}$$

Now $\bar{v}_\theta$ and $\bar{v}_z$ are only functions of r, and ψ and ϕ have a zero ρ average: $P_\rho \psi = P_\rho \phi = 0$.

Velocity potentials have been used by several authors (as Yahata,[18] Kessler,[19] and Marcus[20] in thermal convection), this method being coincident in axisymmetric cases with the stream function formulation (as in Jones[21]). The formulation introduced by Marquès[17] is very well suited in cylindrical geometries, where some subtle problems with the boundary conditions arise, and are solved in the mentioned paper. The authors have applied this method to the thermal convection in vertical cylinders[22] and to the time dependent computation of the spiral flow.[16] We will adopt this formulation, whose main points follow.

The evolution equations for the mean velocities $\bar{v}_\theta$, $\bar{v}_z$ are the averaged θ and z components of the Navier–Stokes equations, and we use the axial components of the curl and double curl of the Navier–Stokes equations for the potentials. Then the incompressibility condition is identically satisfied, and the pressure term is removed from the formulation. A lengthy but straightforward computation gives

$$P_\rho(\hat{\mathbf{e}}_\theta \cdot \Delta \mathbf{v}) = DD_+ \bar{v}_\theta, \qquad P_\rho(\hat{\mathbf{e}}_z \cdot \Delta \mathbf{v}) = D_+ D v_z,$$

$$(1-P_\rho)(\hat{\mathbf{e}}_z \cdot \boldsymbol{\nabla} \times \mathbf{v}) = -\Delta_h \psi,$$

$$(1-P_\rho)(\hat{\mathbf{e}}_z \cdot \boldsymbol{\nabla} \times \Delta \mathbf{v}) = -\Delta \Delta_h \psi,$$

$$(1-P_\rho)(\hat{\mathbf{e}}_z \cdot \boldsymbol{\nabla} \times \boldsymbol{\nabla} \times \mathbf{v}) = \Delta \Delta_h \phi,$$

$$(1-P_\rho)(\hat{\mathbf{e}}_z \cdot \boldsymbol{\nabla} \times \boldsymbol{\nabla} \times \Delta \mathbf{v}) = \Delta \Delta \Delta_h \phi, \qquad (8)$$

where $D = \partial_r$, $D_+ = D + 1/r$, $\Delta_h = D_+ D + r^{-2}\partial_{\rho\rho}^2$, $\Delta = \Delta_h + b^{-2}\partial_{\rho\rho}^2$. For a vector field $\mathbf{A}$ whose cylindrical components depend only on r, ρ, the explicit expression of its curl is given by

$$\boldsymbol{\nabla} \times \mathbf{A} = (-r^{-1}\partial_\rho A_z - b^{-1}\partial_\rho A_\theta, b^{-1}\partial_\rho A_r - \partial_r A_z, D_+ A_\theta$$
$$+ r^{-1}\partial_\rho A_r). \qquad (9)$$

We finally obtain the equations

$$(\partial_t - DD_+)\bar{v}_\theta = -P_\rho(\hat{\mathbf{e}}_\theta \cdot \mathbf{b}), \qquad (10)$$

$$(\partial_t - D_+ D)\bar{v}_z = -P_\rho(\hat{\mathbf{e}}_z \cdot \mathbf{b}), \qquad (11)$$

$$(\partial_t - \Delta)\Delta_h \psi = (1-P_\rho)(\hat{\mathbf{e}}_z \cdot \boldsymbol{\nabla} \times \mathbf{b}), \qquad (12)$$

$$(\partial_t - \Delta)\Delta \Delta_h \phi = -(1-P_\rho)(\hat{\mathbf{e}}_z \cdot \boldsymbol{\nabla} \times \boldsymbol{\nabla} \times \mathbf{b}), \qquad (13)$$

with $\mathbf{b} = \boldsymbol{\omega} \times \mathbf{v} + 2\Omega\hat{\mathbf{e}}_z \times \mathbf{v}$. The corresponding boundary conditions are:

$$\bar{v}_\theta(r_i) = R_i - dr_i^*\Omega/\nu, \bar{v}_\theta(r_o) = R_o - dr_o^*\Omega/\nu,$$
$$\left. \begin{array}{l} \bar{v}_z = D\psi = \phi = \Delta_h \phi = 0 \\ -b\psi + rD\phi = b\Delta\Delta_h\phi + rD\Delta_h\psi = 0 \end{array} \right\} \text{ on } r = r_i, r_o. \qquad (14)$$

The last boundary condition is necessary in order to ensure the equivalence with the Navier–Stokes equation. The velocity potentials are not uniquely determined by the velocity field, so the gauge boundary condition $\phi = 0$ has been used. The remaining boundary conditions come from the no slip condition on the cylinders surface. Using these equations, the computation of the time periodic spiral flow reduces to a two-dimensional (r, ρ) steady problem, in a rotating frame of reference.

The above system of evolution equations were used in Sánchez et al.[16] to calculate the spiral flow by time evolution. Details on the methods used can also be found in Sánchez.[23] Although in this paper we solve the equations (10)–(13) in the steady case, in order to start the continuation method we have used as an initial point a spiral flow obtained by time evolution; the initial guess for Ω is also obtained this way.

III. NUMERICAL METHODS

In order to solve the equations for the potentials we have used spectral methods (Canuto et al.[24]). They have been expanded using Chebyshev polynomials in the radial direction, and a Fourier expansion for the ρ coordinate,

$$\bar{v}_\theta(x) = \sum_{l=0}^{L} f_l T_l(x) \qquad (15)$$

$$\psi(x,\rho) = \sum_{l=0}^{L} \sum_{\substack{n=-N/2 \\ n \neq 0}}^{N/2-1} \psi_{l,n} T_l(x) e^{in\rho}, \qquad (16)$$

and analogous developments for $\bar{v}_z$ and ϕ. $\psi_{l,n}$ are complex numbers but, as ψ is real, they satisfy $\psi_{l,-n} = \psi_{l,n}^*$, so only half of them must be computed.

The discretization of the equations for the potentials is obtained by a Galerkin projection on the periodic coordinate ρ and a collocation method for the radial coordinate x. After the equations are separated into their Fourier components, these are evaluated on a radial mesh of Gauss-Lobatto collocation points. This allows an efficient evaluation of the equations for $\bar{v}_\theta$, $\bar{v}_z$, ψ, and ϕ by using fast Fourier transforms in both coordinates.

Since the spiral flow is now a fixed point in the rotating frame, it can be computed using continuation methods against different parameters. We have used some of the techniques described in Keller,[25] Simó,[26] and Seydel.[27] To fix the phase of the steady solutions in the rotating frame we have added the equation that sets to zero the value of the imaginary part of one of the variables corresponding to the azimuthal dominant mode. This also determines the angular velocity of the rotating frame Ω.

Let p be the continuation parameter (R_i, R_o, or b) and let X be the vector formed with the coefficients of the expansion for $\bar{v}_\theta$, $\bar{v}_z$, ψ, and ϕ [(15)–(16)]. Then the discretized steady Navier-Stokes equations in the rotating frame have the form $F(X, \Omega, p) = 0$. These equations implicitly define a curve of solutions $X = X(p)$, $\Omega = \Omega(p)$. At each stage of the continuation process, from a set of known points on the curve of solutions, a predictor step provides an initial guess from which a corrector step based on a modified Newton–Raphson iteration converges to another point on the curve. For the first two steps the prediction is made using the tangent to the curve. After this startup, polynomial extrapolation is used based on the last three points on the curve.

To start the continuation procedure an initial solution is needed. This is obtained by time evolution of the two-dimensional system for the spirals in a non-rotating reference system in order to attain the periodic regime.

To determine the number of terms needed in the expansions to obtain accurate results, several test have been made. The torques on the inner and outer cylinders have been calculated for different values of the number of terms in both the x and ρ coordinates, and for two values of R_i. The torques on both cylinders must be the same. This has been considered as a precision test by some authors.[13] With the formulation used, the expression for the torque per axial period on the cylinders is

$$M_z(r_\alpha) = 2\pi r_\alpha(\bar{v}_\theta(r_\alpha) - r_\alpha\partial_r\bar{v}_\theta(r_\alpha)), \qquad (17)$$

r_α being the radius of any of the cylinders.

The variation of the angular velocity with the number of terms has also been considered, although this variable is more sensitive than the torque. The variation of the Fourier coefficients of the θ component of $\mathbf{v}$ has also been used as a test. This component has been selected because it is the one of largest magnitude and largest radial variation.

TABLE I. Torque and angular velocity values for $R_i = 150$, $R_o = -50$, $\eta = 0.8$, $b = 0.3055$. (a) $L = 16$ for different N values; (b) $N = 16$ for different L values.

(a)			
N	Inner torque	Outer torque	Angular velocity
12	0.428515E+05	0.428365E+05	0.106146E+02
16	0.426921E+05	0.426924E+05	0.105367E+02
24	0.426993E+05	0.426993E+05	0.105644E+02

(b)			
L	Inner torque	Outer torque	Angular velocity
12	0.426908E+05	0.426912E+05	0.105298E+02
16	0.426921E+05	0.426924E+05	0.105367E+02
24	0.426920E+05	0.426924E+05	0.105368E+02

TABLE II. Torque and angular velocity values for $R_i = 350$, $R_o = -50$, $\eta = 0.8$, $b = 0.3055$. (a) $L = 16$ for different N values, (b) $N = 16$ for different L values.

(a)			
N	Inner torque	Outer torque	Angular velocity
12	0.146235E+06	0.147024E+06	0.292302E+02
16	0.152536E+06	0.152370E+06	0.257615E+02
24	0.151755E+06	0.151752E+06	0.263790E+02

(b)			
L	Inner torque	Outer torque	Angular velocity
12	0.156284E+06	0.156106E+06	0.276747E+02
16	0.152536E+06	0.152370E+06	0.257615E+02
24	0.151834E+06	0.151653E+06	0.245542E+02

In Tables I–III the results of some of the precision tests are summarized. All parameters have been fixed except R_i for which two different values have been considered. Both values, 150 and 350, are above the region where spirals are stable but have been selected because spirals ranging from $R_i = 110$ to $R_i = 500$ will be analyzed later. The remaining parameters are $R_o = -50$, $\eta = 0.8$, and $b = 0.3055$. In Table I(a) the inner and outer torques and the angular velocity of the spirals are shown for $R_i = 150$, $L = 16$, and $N = 12,16,24$. Table I(b) shows the same results but for fixed $N = 16$ and $L = 12,16,24$. The same results are reproduced in Tables II(a) and II(b) for $R_i = 350$.

From Table I it is clear that using $L = 16$ and $N = 16$ is enough to have torques that differ in the sixth digit and whose four first digits do not change when N is increased to 24. For the angular velocity the difference between the values for $N = 16$ and $N = 24$ are in the fourth digit. Table II shows that keeping $N = 16$ and varying L gives better convergence; both torques and angular velocity differ in the sixth digit when $L = 16$ and $L = 24$. The best results for the torques are easy to understand because from Eq. (17) M_z only depends on r. The results for $R_i = 350$ shows an error less than 0.5% for torques and less than 5% for the angular velocity, taking $L = N = 16$ modes. As has been stated above, we see that the angular velocity Ω is specially sensitive.

In Table III the extreme values of the Fourier coefficients for the azimuthal velocity are shown. After calculating the velocity field from (6), v_θ can be written as

TABLE III. Extrema of Fourier amplitudes of v_θ. $R_o = -50$, $\eta = 0.8$, $b = 0.3055$, (a) $L = 16$ and for different N values. (b) $N = 16$ and for different L values.

(a)				
	$R_i = 150$		$R_i = 350$	
Mode	$N = 16$	$N = 24$	$N = 16$	$N = 24$
0	−0.271672E+02	−0.271671E+02	−0.126811E+03	−0.127297E+03
1	−0.170339E+02	−0.170332E+02	−0.267587E+02	−0.284028E+02
2	−0.336842E+01	−0.336884E+01	0.793644E+01	0.893874E+01
3	0.105391E+01	0.105375E+01	0.643908E+01	0.526421E+01
4	0.106183E+00	0.106166E+00	−0.264487E+01	−0.120163E+01
5	−0.119893E+00	−0.119847E+00	0.228243E+01	0.176808E+01
6	0.210001E−01	0.209143E−01	−0.158626E+01	−0.146373E+01
7	0.813100E−02	0.680715E−02	0.116448E+01	0.880084E+00
8		−0.258144E−02		−0.482239E+00
9		0.205742E−03		0.223266E+00
10		0.175274E−03		−0.890696E−01
11		−0.346771E−04		0.274590E−01

(b)				
	$R_i = 150$		$R_i = 350$	
Mode	$L = 16$	$L = 24$	$L = 16$	$L = 24$
0	−0.271672E+02	−0.278698E+02	−0.126810E+03	−0.125971E+03
1	−0.170339E+02	−0.172286E+02	−0.267587E+02	−0.267387E+02
2	−0.336842E+01	−0.336914E+01	0.793644E+01	0.791733E+01
3	0.105391E+01	0.105424E+01	0.643908E+01	0.657595E+01
4	0.106183E+00	0.111624E+00	−0.264487E+01	−0.298387E+01
5	−0.119893E+00	−0.119434E+00	0.228243E+01	0.241191E+01
6	0.210001E−01	0.214979E−01	−0.158626E+01	−0.153259E+01
7	0.813100E−02	0.815212E−02	0.116448E+01	0.102392E+01

$$v_\theta(x,\rho) = \sum_{l=0}^{L} \sum_{n=-N/2}^{N/2-1} v_{\theta_{l,n}} T_l(x) e^{in\rho}, \qquad (18)$$

and its Fourier modes are defined as

$$v_{\theta_n}(x) = \sum_{l=0}^{L} v_{\theta_{l,n}} T_l(x). \qquad (19)$$

The coefficients displayed in Table III are

$$\max_i v_{\theta_n}(x_i) \quad \text{or} \quad \min_i v_{\theta_n}(x_i), \quad i=0, \dots, L, \qquad (20)$$

depending on which is larger in absolute value, and being $x_i = \cos(i\pi/L)$ the radial Gauss–Lobatto collocation points. As a measure of the precision we will use the maximum error in the six dominant modes, because they account for 99% of the amplitude in the worst case considered. The error in a physical variable is much smaller, because the maximum error considered appears in high modes ($n > 3$).

In Table III the coefficients for both cases $R_i = 150$ and $R_i = 350$ are shown. As for the torques, for $R_i = 150$, keeping $L = 16$ the three leading digits (error less than 0.5%) of the six dominant modes do not change when N is increased from 16 to 24. The convergence when N is kept to 16 and L is increased is not so good (less than 5%) indicating that better resolution on the radial direction is needed. The same can be seen for $R_i = 350$, with errors less than 12%. The presence of narrow boundary layers near the cylinders for high R_i explains why it is necessary to increase the number of radial modes. For this reason, in all subsequent calculations shown later we have used $L = 24$ and $N = 16$.

Because we have only studied qualitative properties of spirals for high R_i we consider the results accurate enough. For the spirals experimentally observable below $R_i = 150$ the numerical results are very accurate.

IV. THE SET OF SOLUTIONS

As there are many parameters in the problem, we have limited our study to the case $\eta = 0.8$, and since changing b to $-b$ corresponds to a reflexional symmetry with respect to a plane perpendicular to the axis of the cylinders, only positive values of b have been used.

The primary instabilities and bifurcation curves for the circular Couette flow in the counter-rotating case were computed and compared with experiments by Langford *et al.* in 1988.[28] They found that for moderate outer Reynolds number R_o in the counter-rotating case, the transition to spirals take place with an azimuthal wave number $n = 1$. For increasing negative values of R_o, the critical azimuthal wave number is $n = 2,3, \dots$. They also noticed that solutions corresponding to different values of n have identical qualitative properties. Sánchez, Crespo, and Marquès[16] have computed numerically by time evolution spiral flows for different dominant n modes, and have found analogous results. Therefore, we have selected the parameters to ensure that the azimuthal dominant mode is always $n = 1$.

Figure 1(a) shows a typical representation of the solutions obtained by continuation methods. We have plotted $A_{01} = \text{sign}(\text{Re}\psi_{0,1})|\psi_{0,1}|$, the absolute value of the amplitude
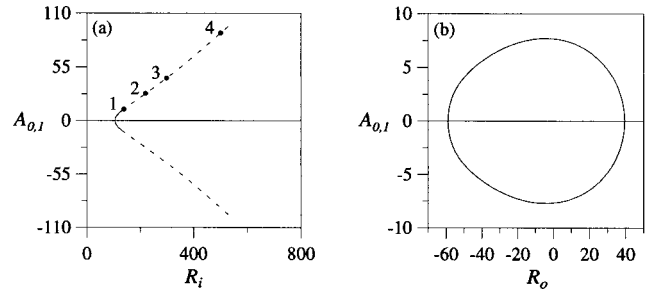

FIG. 1. Branches of spiral flow. (a) Inner Reynolds number R_i as parameter, $b = 0.3055$, and $R_o = -50$. (b) Outer Reynolds number R_o as parameter, $b = 0.3055$, and $R_i = 110$.

$\psi_{0,1}$ times the sign of its real part, versus the inner Reynolds number R_i for $R_o = -50$ and $b = b_{crit} = 0.3055$. This value of b has been taken from the linear stability analysis (Langford *et al.*[28] and Sánchez *et al.*[16]). At this value the inner Reynolds number at which Couette flow becomes unstable has a minimum. At this point $R_i = 106.1$, a Hopf bifurcation occurs and the periodic spiral regime appears.

As a result of working in the rotating frame where the spiral is at rest, a one parameter family of steady solutions can be found. Two of these solutions differ only by a phase shift or a rotation around the axis of the cylinders. This is why the sign of the real part of the variable plotted in Figs. 1–2 has been included. The real part can be positive or negative, giving the two symmetrical branches shown. These two solutions differ only by a rotation around the axis of the cylinders of 180 degrees. The horizontal line represents the Couette flow. No other helical symmetric solutions branching from the spiral regime were found in our calculations, except the Couette flow. The branch has been calculated for inner Reynolds numbers above those for which experiments show that spirals become unstable, in order to study the spiral properties for high Reynolds number R_i, and to search for bifurcations that still retain the spiral invariance. The stability of this branch is given by the eigenvalues of the Jacobian matrix of the system, which is computed throughout the continuation procedure. We found a secondary Hopf bifurcation at $R_i = 137.2$. In the non-rotating reference frame, the flow is quasiperiodic. In a previous paper,[16] we already found bifurcations to a quasiperiodic regime by time evolution of the Navier–Stokes equations with helical symmetry. We showed that the presence of a quasiperiodic flow near the
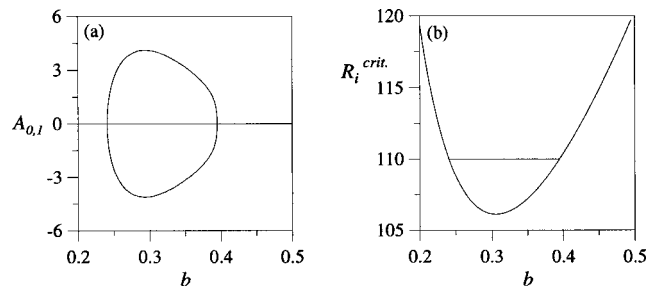

FIG. 2. (a) Branches of spiral flow depending on the parameter b. (b) Marginal stability curve of the transition from circular Couette flow to spiral flow.
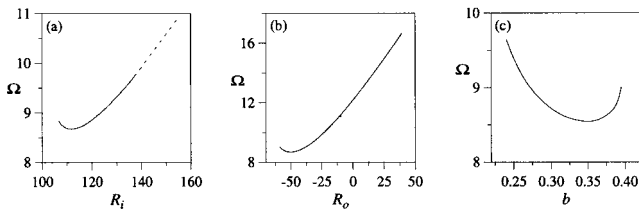
FIG. 3. Angular velocity Ω of the spiral pattern along the continuation paths using as parameters (a) the inner Reynolds number R_i, (b) the outer Reynolds number R_o, and (c) the spiral slope b. The values of the parameters held constant are $R_i = 110$, $R_o = -50$, $b = b_{crit} = 0.3055$.

primary instability was caused by the competition between different spiral modes, with the same parameter b but different azimuthal dominant mode n. We have plotted the unstable branches with dashed lines, in Figs. 1 and 3.

Figure 1(b) shows the curve of solutions obtained when the outer Reynolds number is used as a parameter from a solution slightly above the critical inner Reynolds number. For this plot $R_i = 110$, $b = b_{crit} = 0.3055$ as before, and the initial condition is taken from the other curve with $R_o = -50$. The horizontal line again corresponds to Couette flow. We may now observe that solutions exist only for a limited range of outer Reynolds numbers (between -58.90 and 39.46 in this plot), including positive values. This indicates the existence of spirals in the co-rotating case that are not observed in experiments because Couette flow first bifurcates to axisymmetric Taylor vortices, and probably because these spiral solutions (for $R_o > 0$) are unstable to non-helical perturbations. All the branch is stable against perturbations with helical symmetry. As the stability of these solutions against 3-dimensional perturbations has not been studied it is impossible to establish if they are stable along all the curve or not. If they were stable they should be observed in experiments at a certain interval above $R_o = -50$ by moving the system from a counter-rotating stable spiral state to co-rotation simply by varying the outer Reynolds number.

The lower limit is $R_o = -58.90$ where the flow bifurcates to Couette flow. The critical R_i and b for $R_o = -58.90$ are $R_i^{crit} = 109.99 < 110.00$ and $b^{crit} = 0.3019$, so the plotted curve of solutions ends very near the critical curve from Couette flow to spirals but not exactly because of the different values of b.

The symmetry of the curve is again related to a 180 degree rotation around the axis of the cylinders, and in this case the curve crosses the two-dimensional variety of Couette flow solutions (parametrized by the two Reynolds numbers, for fixed b) twice.

The left plot in Fig. 2 shows the curve of solutions obtained when b is used as continuation parameter, for fixed $R_i = 110$, $R_o = -50$. The set of values of b for which spirals exist is limited by the stability curve of Couette flow, as can be seen in Fig. 2. The parabolic curve corresponds to the transition from Couette flow to an spiral of dominant azimuthal number $n = 1$. The horizontal line at $R_i = 110$ is the projection onto this plot of the curve of solutions depending on b. As the inner Reynolds number is increased, the interval of possible slopes for the spirals is wider. A stability analysis

of the spirals would reveal a curve inside the transition one from Couette flow, indicating the interval of allowed b as in the case of Taylor vortices for the axial wavelength.

The symmetry of the curve is related again to a 180 degree rotation around the axis of the cylinders, and the curve crosses the one-dimensional variety of Couette flow solutions (parametrized this time by b for the two Reynolds numbers fixed) twice.

For fixed R_i, the region in the (R_o, b) space where the spiral flow exists is bounded. The b values are limited by the critical curve corresponding to the transition from Circular Couette Flow (CCF) to Spiral flow, as shown in Fig. 2 right. R_o is limited because for $R_o = R_i/\eta > 0$ the rigid body rotation case CCF is absolutely stable. For negative and large R_o, the outer rotation has a stabilizing effect,[29] so the spiral flow appears for higher and higher R_i. For very large and negative R_o values ($R_o < -2 \times 10^4$), other mechanisms of instability appear, characterized by intermittency, hysteresis, and regions of turbulent flow. Coles[30] used the term *catastrophic transition* for these processes. They appear far from the parameter range we study here.

V. SPIRAL FLOW PROPERTIES

In Fig. 3 the dependence of the angular velocity of the pattern has been plotted versus different continuation parameters. It increases with the inner Reynolds number, except at the very beginning of the branch where a slight decrease can be noticed. The second curve (R_o continuation) has a minimum at $R_o = -50$, and the third also has a minimum at $b = 0.3486$. If this last curve is compared with the stability curve in Fig. 2, it can be seen that the preferred b at the onset of instability from Couette flow, $b = 0.3055$, is not the one that makes the angular velocity minimum. In fact, the preferred value $b = 0.3055$ makes the axial period 1.92, nearly twice the gap between cylinders, as in the transition to Taylor vortices.

We now consider the properties of the spirals labeled 1, 2, 3, 4 in the plot in Fig. 1 corresponding to inner Reynolds numbers 140, 220, 300, and 500, respectively. The behavior of the mean flows is displayed in Fig. 4. In Fig. 4(a) we see that when the inner Reynolds number is increased, two boundary layers develop near the walls, where the fluid is dragged by the wall rotation, and the fluid in the center of the cylinders has nearly zero average azimuthal velocity; it is almost at rest in the rotating reference system. Figure 4(c) shows the net azimuthal flux in the rotating reference system. It is small and increases with R_i until saturation near the spiral flow labeled 2. Figure 4(b) shows that there are nonzero mean axial flows with opposite signs near each cylinder. This gives a large scale motion on the z axis. Moreover, these mean axial flows do not compensate each other: a net mass flux appears in the axial direction, as shown in Fig. 4(d). This net flux changes sign when the Reynolds number is increased.

The presence of a weak but not zero axial mass flow has been pointed out by Edwards *et al.*[6] This is a purely nonlinear effect; it can easily be seen (Sánchez, Crespo, and Marquès[16]) that the linear eigenfunction that appears in the
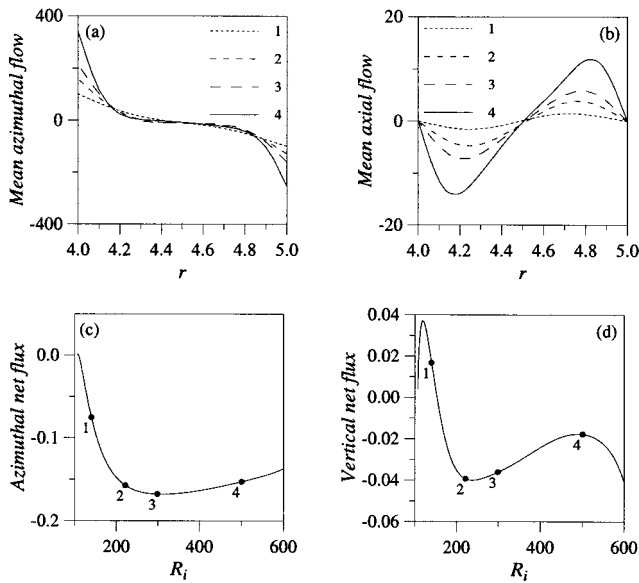
FIG. 4. (a), (b) mean flows in the azimuthal and axial directions. (c), (d) the corresponding net flux normalized with the net azimuthal flux of the basic Couette flow.
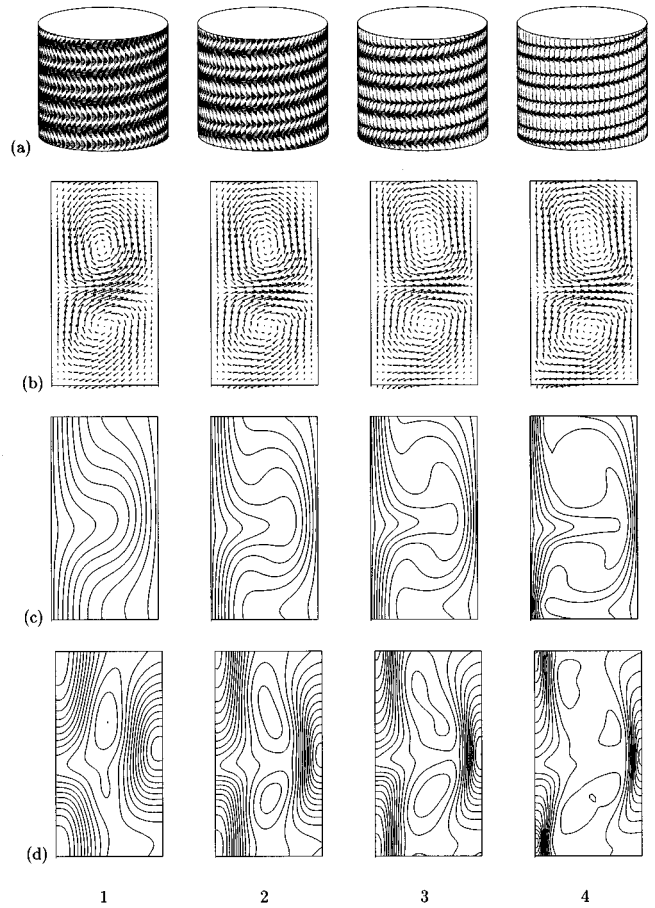

FIG. 5. (a) Perspective of the velocity field for the mean radius. (b) Velocity field at a vertical plane. (c) Isolines of azimuthal velocity. (d) Isolines of vertical vorticity. The four plots in each case correspond to the spirals 1, 2, 3, and 4 along the R_i continuation curve of Fig. 1.

bifurcation has zero mean flows $\bar{v}_\theta$, $\bar{v}_z$, and therefore zero axial mass flow. This feature is not present in the Taylor vortex flow, but appears in the spiral flow in an axially periodic domain as a result of the reflexional ($z \to -z$) symmetry breaking bifurcation from which the SF emerges. Spirals with opposite values of b are symmetric with each other and have opposite axial mass flow.

In Fig. 5 the global structure of the flow can be seen. On top of Fig. 5 a perspective view of the velocity field for the mean radius is shown. The flow looks sinusoidal near the transition, but for high Reynolds number the center of the vortices is almost at rest, as the mean flows also show. This suggests that the core of the vortices tends to move like a rigid body, and in the rotating reference frame they are virtually at rest. This rigid body rotation is confirmed by the last line of plots (isolines of vertical vorticity), which shows that the vertical vorticity in the center is almost constant (in fact nearly zero). These results support the theoretical model proposed by Batchelor,[31] which is based on the assumption that, for $R_i \to \infty$, the secondary flow in the axial plane consists of an inviscid core surrounded by boundary layers.

Figure 5(b) shows the velocity field in a θ constant section. When the Reynolds number increases, we see the formation of an outgoing jet. Figure 5(c) shows the isolines of the azimuthal velocity, confirming the formation of the aforementioned jet, which keeps the angular momentum up to collide with the outer wall. Boundary layers appear near the walls and between the vortices.

These results are similar in many aspects to those obtained by Fasel and Booz,[13] for the Taylor Vortex Flow (TVF) at high Reynolds numbers. The evolution of a jetlike or shocklike flow structures, boundary layers developing near the walls, and the nearly inviscid behavior of the core region for large Reynolds numbers, are very similar in both SF and TVF. The differences are due to the lack of the re-

flexional ($z \to -z$) symmetry: the vortices come in pairs of different size, and a net axial mass flow appears.

VI. STREAM FUNCTION AND TRAJECTORIES

To describe the trajectories of the velocity field of the spirals, we find a first integral of the field from the incompressibility condition. In the case of Taylor vortices, the trajectories are easy to describe. The projections of the streamlines in an $r-z$ plane are closed curves, so the full streamlines lie on toroidal surfaces and almost all are dense and describe a quasiperiodic motion (see Ashwin and King[32]). The situation in the case of the spirals is different because the stream function depends on the three coordinates. If expressed in terms of the ρ coordinate it is possible to describe completely the set of trajectories.

The incompressibility condition written in the (r, ρ) coordinates for the spiral flow is

$$\frac{1}{r}\partial_r(rv_r) + \partial_\rho\left(\frac{v_z}{b} - \frac{v_\theta}{r}\right) = 0. \tag{21}$$

The boundary conditions say that the radial flux is zero, and this condition guarantees the existence of a stream function $\chi(r,\rho,t)$ such that
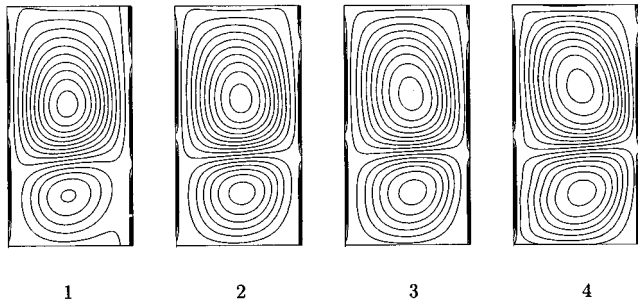
FIG. 6. Intersection of the integral surfaces $\chi =$const, with a vertical plane $\theta =$const. (a), (b), (c) correspond to the spirals 1, 2, 3 along the R_i continuation curve of Fig. 1.

FIG. 7. Axial shift per unit time corresponding to the spiral number 1. The horizontal coordinates are (r,ρ).

$$v_r = -\frac{1}{r}\partial_\rho\chi, \quad v_\rho = \frac{v_z}{b}-\frac{v_\theta}{r} = \frac{1}{r}\partial_r\chi \Rightarrow \frac{d\chi}{dt} = \partial_t\chi. \quad (22)$$

However, in the rotating frame the velocity field is steady, and therefore the stream function does not depend explicitly on time. In this case $d\chi/dt=0$ and the particle trajectories lie on the surfaces $\chi =$constant. These integral surfaces are invariant by a helical symmetry, and can be obtained from the curves $\chi =$constant in the (r,z) plane by a helical movement. Figure 6 shows the $\chi =$constant curves at the 1, 2, 3, and 4 aforementioned points. Notice that a vertical plane (r,z) defined by $\theta =$constant, is the same as a plane in the (r,ρ) coordinates, due to $\rho = z/b - \theta$. In the initial non-rotating reference frame these integral surfaces also exist, but they are not steady and they rotate around the z-axis with the angular velocity Ω of the spiral pattern.

The stream function has a very simple expression in terms of the velocity potentials;

$$\chi(r,\rho) = \psi - \frac{r}{b}\phi_r + H(r), \quad H(r) = \int_{r_i}^{r}\left(\frac{r}{b}\bar{v}_z - \bar{v}_\theta\right)dr,$$
$$(23)$$

where the contribution of the mean flows is in the H term.

A detailed description of the particle trajectories can be obtained from the stream function. Looking at Fig. 6, we see that the (r,ρ) coordinates of a particle trajectory are periodic in time, except for the fixed points and homoclinic trajectories described below. The period is the time taken to go over a χ-constant curve; notice that ρ being periodic, we may identify the top $(\rho =2\pi)$ and bottom $(\rho =0)$ of the plots in Fig. 6. In a period, however, the z coordinate may not recover its initial value, and undergoes a shift both in the axial and azimuthal directions. When the particle comes back to the starting point $\Delta\rho =0$ but, as $\rho = z/b - \theta$ (3), $\Delta z = b\Delta\theta$ $\neq 0$ in general. Both the axial shift $\Delta z(\chi)$ and the period $T(\chi)$ depend on the value of χ on the χ-constant curve considered.

There are four fixed points in the plot of the level curves of $\chi =$constant (Fig. 6), defined by $v_r=v_\rho=0$: two centers in the middle of the vortices, and two saddle points on the sides of the small vortex (see Fig. 8). Joining the saddle points to themselves there are four homoclinic loops, depicted in Fig. 8. For the fixed points, the period is zero, but
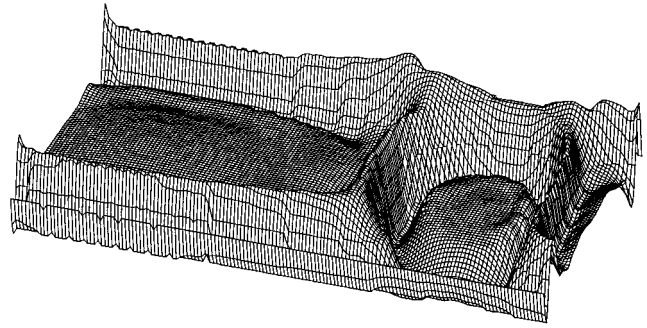
$v_z\neq 0$ in general, so the particles in these points can have an axial motion. On the homoclinic loops, the period goes to infinity, as the particle tends to the saddle points; the axial motion of a particle in one of this homoclinic trajectories tend to be the same as the saddle points for large times.

The axial shift per unit time $\Delta z(\chi)/T(\chi)$ is shown in Fig. 7 as a function of (r,ρ). We notice that the center of the vortices is at rest and that the axial motion takes place in the boundary layers near the walls and between the vortices, inside the jetlike structures described in Sec. V. As we have already mentioned, the stream function has two saddle points near the walls. Surprisingly, the axial motion is confined mainly near and between the homoclinic curves joining the saddle points. The shape of these curves can be seen in Fig. 8 for the 1, 2, 3 cases.

Another striking fact is that these curves tend to merge when the Reynolds number R_i increases. In fact, for the spiral labeled 3 in Fig. 1(a), they are almost identical, and the same happens for the spiral labeled 4 (not depicted). Therefore the axial motion is concentrated in an internal boundary layer that becomes very narrow at high Reynolds number. In any case, this axial motion is very small compared with the azimuthal velocities of the flow, as Fig. 4 shows.

Figures 9, 10 and 11 show different views of the particle paths in case 1, corresponding to three of the five regions in
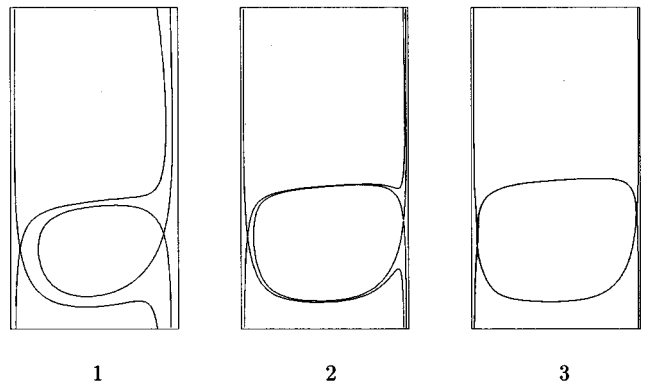

FIG. 8. Homoclinic trajectories of the stream function in a $\theta =$const plane. (a), (b), (c) correspond to the spirals 1, 2, 3 along the R_i continuation curve of Fig. 1.
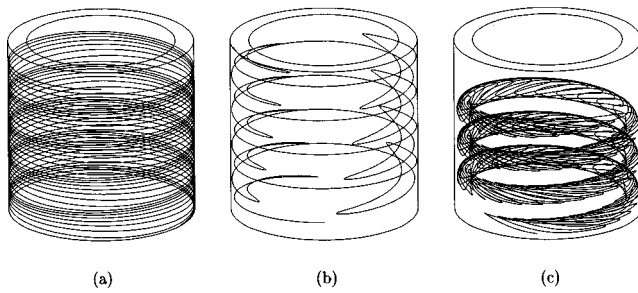
FIG. 9. Trajectories; perspective view. (a) Initial point near the inner cylinder. (b) Initial point between the homoclinic curves. (c) Initial point near the center of a vortex.

FIG. 11. Trajectories; top view. (a), (b), (c) are the same as in Fig. 9.

which the homoclinic curves separate an $r-z$ period. Plot (a) in each figure corresponds to particles near the outer cylinder; the corresponding integral surfaces are nearly cylinders parallel to the walls. Plot (b) corresponds to a particle path confined between the homoclinic curves, and plot (c) to trajectories inside the bigger spiral vortex. In this last case the integral surfaces are spiral tubular surfaces [see Fig. 9(c)]. Other trajectories, near the inner cylinder or inside the smallest vortex, look similar to plots (a) and (b), respectively.

Figure 10 shows the axial displacement of the particles. It is clear that for trajectories between the homoclinic curves of the stream function, the vertical displacement is greater than for any other: in a few periods they escape from the depicted region. The axial drift of the trajectories in the first and third cases decreases if the particle is closer to the walls or to the center of the vortices. Figure 11 shows the radial displacement of the particles: If a particle is near any of the cylindrical surfaces it remains there. The others travel from cylinder to cylinder. The time a particle remains near one of the two walls before leaving it is greater for the second kind of paths, corresponding to trajectories confined between the homoclinic trajectories.

VII. CONCLUSIONS AND PERSPECTIVES

In this paper we have computed the spiral flow by introducing two space coordinates adapted to the symmetry of the flow, and using continuation methods in the rotating reference system where the SF is steady. So we have obtained a highly efficient computation scheme, reducing the 3D time dependent flow to the computation of a steady 2D one. The continuation method allows us to compute this flow even though it is unstable. We have found that the SF exists in a
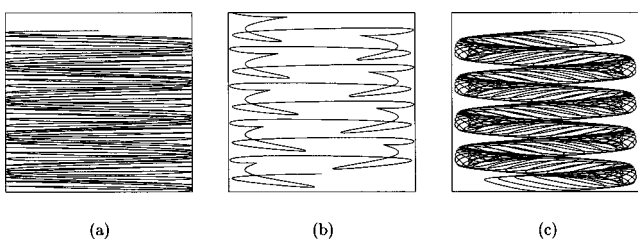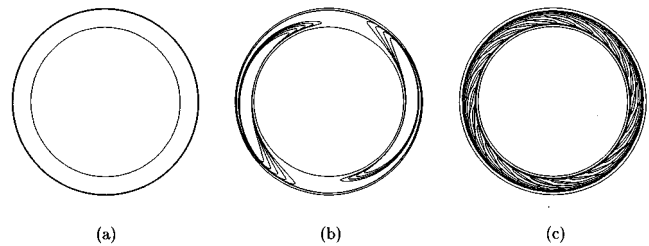
much wider parameter range than experiments suggest. In particular, it also exists in the corotating case. We have made a limited linear stability analysis of the spiral flow, restricted to perturbations with helical symmetry. Even in this case, the spirals are only stable in a small range of the inner Reynolds number R_i.

The analysis of the flow properties shows some features very close to the ones corresponding to TVF, such as the formation of jetlike structures and the appearance of an inviscid core for high Reynolds number R_i, in agreement with Batchelor's theory. The main differences are due to the breaking of the reflexional symmetry $z \rightarrow -z$. As a result the SF is made of couples of unequal vortices, and an axial mean flow giving a net axial mass flux appears.

As a result of the helical symmetry of the flow, we have found a first integral of the velocity field, which provides us with a detailed description of the particle trajectories in the flow. This description shows that the axial motion is mainly confined in a region near and between two homoclinic integral surfaces, which coincide with the boundaries of the spiral vortices and contain the inflow and outflow radial jets. This region, where the axial motion takes place, shrinks to zero for high Reynolds number. This internal boundary layer concentrates most of the axial and radial motions of the particles.

Instabilities of this boundary layer (like jet instabilities) can be one of the instability mechanisms of the spiral flow. Other forms of instability, such as competition between different modes, have also been suggested by Sánchez, Crespo, and Marquès.[16] In future work we need to address the question of the stability of the spiral flow, the mechanisms of instability that appear, and their relationship with the SF properties displayed in this work. This linear stability analysis will greatly benefit from the highly efficient SF computational methods introduced in this paper.

FIG. 10. Trajectories; frontal view. (a), (b), (c) are the same as in Fig. 9.

[1] R. Tagg, ''A guide to the literature related to the Taylor-Couette problem,'' in *Ordered and Turbulent Patterns in Taylor–Couette Flow,* edited by C. D. Andereck and F. Hayot (Springer-Verlag, New York, 1992).
[2] J. T. Stuart, ''On the non-linear mechanics of hydrodynamic stability,'' J. Fluid Mech. **4**, 1 (1958).
[3] A. Davey, ''The growth of Taylor vortices in flow between rotating cylinders,'' J. Fluid Mech. **14**, 336 (1962).

[4]W. C. Reynolds and M. C. Potter, ''Finite-amplitude instability of parallel shear flows,'' J. Fluid Mech. **27**, 465 (1967).

[5]K. Kirchgässner and P. Sorger, ''Branching analysis for the Taylor problem,'' Q. J. Mech. Appl. Math. **22**, 183 (1966).

[6]W. S. Edwards, R. P. Tagg, B. C. Dornblaser, and H. L. Swinney, ''Periodic traveling waves with nonperiodic pressure,'' Eur. J. Mech. B Fluids **10**, 205 (1991).

[7]G. Iooss, ''Secondary bifurcations of Taylor vortices into wavy inflow or outflow boundaries,'' J. Fluid Mech. **173**, 273 (1986).

[8]Y. Demay and G. Iooss, ''Calcul des solutions bifurquées pour le problème de Couette-Taylor avec les deux cylindres en rotation,'' J. Méc Théor. Appl, Numéro spécial, 193–216.

[9]P. Chossat and G. Iooss, *The Couette–Taylor Problem* (Springer-Verlag, New York, 1994).

[10]R. Meyer-Spasche and H. B. Keller, ''Computation of the axisymmetric flow between rotating cylinders,'' J. Comput. Phys. **35**, 100 (1980).

[11]R. Meyer-Spasche and H. B. Keller, ''Some bifurcation diagrams for Taylor vortex flows,'' Phys. Fluids **28**, 1248 (1985).

[12]N. Dinar and H.B. Keller, ''Computation of Taylor vortex flows using multigrid continuation methods,'' in *Recent Advances in Computational Fluid Dynamics*, edited by C. C. Chao, S. A. Orszag, and W. Shyy (Springer-Verlag, New York, 1989), pp. 191–262.

[13]H. Fasel and O. Booz, ''Numerical investigation of supercritical Taylor-vortex flow for a wide gap,'' J. Fluid Mech. **138**, 21 (1984).

[14]P. S. Marcus ''Simulation of Taylor–Couette flow. Part 1. Numerical methods and comparison with experiments,'' J. Fluid Mech. **146**, 45 (1984).

[15]P. S. Marcus ''Simulation of Taylor–Couette flow. Part 2. Numerical results for wavy-vortex flow with one traveling wave,'' J. Fluid Mech. **146**, 65 (1984).

[16]J. Sánchez, D. Crespo, and F. Marquès, ''Spiral vortices between concentric cylinders,'' Appl. Sci. Res. **51**, 55 (1993).

[17]F. Marquès, ''On boundary condition for velocity potentials in confined flows: Application to Couette flow,'' Phys. Fluids A **2**, 729 (1990).

[18]H. Yahata, ''Competition of the two unstable modes in the Rayleigh–Bernard convection,'' Prog. Theor. Phys. **78**, 282 (1987).

[19]R. Kessler, ''Nonlinear transition in three-dimensional convection,'' J. Fluid Mech. **174**, 357 (1987).

[20]P. S. Marcus, ''Effects of truncation in modal representations of thermal convection,'' J. Fluid Mech. **103**, 241 (1981).

[21]C. A. Jones, ''On flow between counter-rotating cylinders,'' J. Fluid Mech. **120**, 433 (1982).

[22]F. Marquès, M. Net, J. Massaguer, and I. Mercader, ''Thermal convection in vertical cylinders. A method based on potentials of velocity,'' Comput. Methods Appl. Mech. Eng. **110**, 157 (1993).

[23]J. Sánchez, ''Simulacion numerica en flujos confinados: estructuras pre-turbulentas,'' Ph.D. thesis, Universitat de Barcelona, I.S.B.N. 84-475-0945-1, 1994.

[24]C. Canuto, M.Y. Hussaini, A. Quarteroni, and T.A. Zang, *Spectral Methods in Fluid Dynamics* (Springer-Verlag, New York, 1987).

[25]H. B. Keller, ''Numerical solution of bifurcation and nonlinear eigenvalue problems,'' in *Applications of Bifurcation Theory*, edited by P. H. Rabinowitz (Academic, New York, 1977).

[26]C. Simó, ''On the analytical and numerical approximation of invariant manifolds,'' in *Modern Methods in Celestial Mechanics*, edited by D. Benest and C. Froeschlé (Editions Frontières, Paris, 1990).

[27]R. Seydel, *Practical Bifurcation and Stability Analysis* (Springer-Verlag, New York, 1994).

[28]W. F. Langford, R. Tagg, E. J. Kostelich, H. L. Swinney, and M. Golubitsky, ''Primary instabilities and bicriticality in flow between counter-rotating cylinders,'' Phys. Fluids **31**, 776 (1988).

[29]C. D. Andereck, S. S. Liu, and H. L. Swinney, ''Flow regimes in a circular Couette system with independently rotating cylinders,'' J. Fluid Mech. **164**, 155 (1986).

[30]D. Coles, ''Transition in circular Couette flow,'' J. Fluid Mech. **21**, 385 (1965).

[31]G. K. Batchelor, ''On steady laminar flow with closed streamlines at large Reynolds number,'' J. Fluid Mech. **1**, 177 (1956).

[32]P. Aswin and G. P. King, ''A study of particle paths in non-axisymmetric Taylor–Couette flows,'' J. Fluid Mech. **338**, 341 (1997).